Building Fluorescence Lifetime Maps Photon-by-Photon by Leveraging Spatial Correlations

Mohamadreza Fazel, Sina Jazani, Lorenzo Scipioni, Alexander Vallmitjana, Songning Zhu, Enrico Gratton, Michelle A. Digman, and Steve Pressé*

Read Online
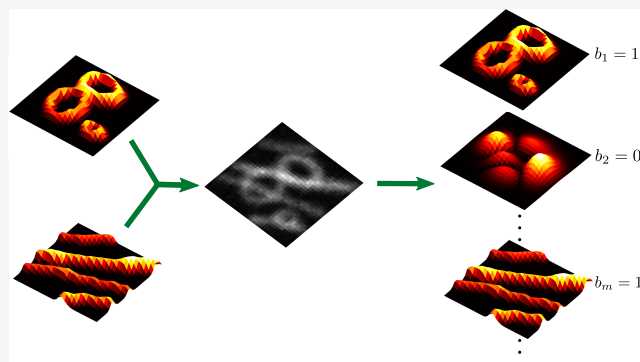
ACCESS | Metrics & More | Article Recommendations | Supporting Information

ABSTRACT: Fluorescence lifetime imaging microscopy (FLIM) has become a standard tool in the quantitative characterization of subcellular environments. However, quantitative FLIM analyses face several challenges. First, spatial correlations between pixels are often ignored as signal from individual pixels is analyzed independently thereby limiting spatial resolution. Second, existing methods deduce photon ratios instead of absolute lifetime maps. Next, the number of fluorophore species contributing to the signal is unknown, while excited state lifetimes with <1 ns difference are difficult to discriminate. Finally, existing analyses require high photon budgets and often cannot rigorously propagate experimental uncertainty into values over lifetime maps and number of species involved. To overcome all of these challenges simultaneously and self-consistently at once, we propose the first doubly nonparametric framework. That is, we learn the number of species (using Beta-Bernoulli process priors) and absolute maps of these fluorophore species (using Gaussian process priors) by leveraging information from pulses not leading to observed photon. We benchmark our framework using a broad range of synthetic and experimental data and demonstrate its robustness across a number of scenarios including cases where we recover lifetime differences between species as small as 0.3 ns with merely 1000 photons.

KEYWORDS: lifetime imaging, FLIM, confocal, Bayesian, Gaussian process, Beta-Bernoulli

INTRODUCTION

Among many fluorescence microscopy techniques,[1−7] fluorescence lifetime imaging microscopy[1,2] (FLIM) has been pivotal in elucidating static properties and chemical interactions occurring within subcellular environments, fluids, and solid materials.[8−27] For example, FLIM has been employed in deducing nanoscale maps of optical,[9,11−13] thermodynamic,[14−21] and chemical parameters.[22−26] Furthermore, FLIM has also been employed in drug discovery to monitor drug activity within complex biological environments.[28,29]

In typical FLIM experiments, data consist of a series of photon arrival times, following laser pulses whose statistics are dictated by the present number of fluorophore species and excited state lifetime. Photon arrival times can then be decoded to learn the number of fluorophore species, as well as their associated lifetimes. In imaging across regions of space, we may also decode the corresponding lifetime maps.
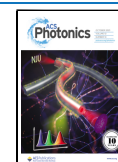
Here, we assume that the input arrival times (the FLIM data) are collected by using a scanning confocal setup. In this setup, a pulsed laser, often with a Gaussian waist, scans the sample at a constant speed over uniformly spaced horizontal trajectories, where the spacing defines the pixel size. The excited fluorophores then emit photons with a random delay

drawn from a distribution characteristic of the fluorophore species, Figure 1a. Moreover, the recorded arrival times are further contaminated with instrumental noise. That is: (1) the detector delay in recording the arrival times and (2) the unknown exact time of excitation due to the finite breadth of excitation pulses. Together, these are often modeled using a Gaussian distribution, termed the instrumental response function (IRF). The exponential waiting time of de-excitation for each fluorophore species and the effects of the IRF thus result in two layers of stochasticity in reported photon arrival times given by the convolution of the exponential and IRF distributions.

To learn the number of fluorophore species as well as their associated lifetimes from FLIM data, the community relies either on model-free methods, such as phasor-based approaches[30−33] and neural networks,[34−36] or on model-
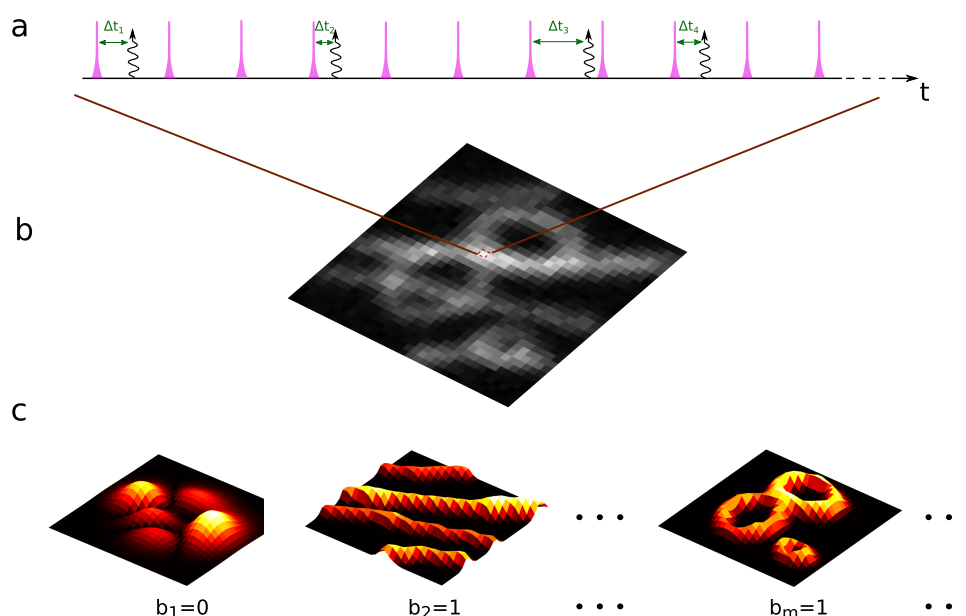
Figure 1. Cartoon illustration of a typical FLIM experiment and the BNP-FLIM framework. (a) Every spot in the specimen is illuminated by a train of laser pulses, designated by pink spikes, where a fraction of them lead to the detection of photons, shown by curly arrows. The photon arrival times, Δt_k, are recorded and used in FLIM analysis to infer the number of fluorophore species as well as their associated spatial maps and corresponding lifetimes. (b) The sets of photons drawn from all spots are arranged into a two-dimensional pixel array representing the raw FLIM data. (c) The Bayesian nonparametric FLIM (BNP-FLIM) framework models the input data (nominally) assuming an infinite number of species. To each species are associated a nominally infinite number of candidate spatial maps for how the fluorophores are distributed. Eventually, as shown in (c), our method determines: (1) which species are warranted by the data (for which the associated Bernoulli variable, b, is found to be unity) and what its lifetime is and (2) its associated lifetime map. In the case shown in (c), only the second and mth species are warranted by the data and have a nonzero associated Bernoulli variable b (i.e., $b_2 = b_m = 1$). The map determined for the first species (with $b_1 = 0$) is thus immaterial.

based methods such as FLIM data analysis techniques including time-correlated single photon counting (TCSPC) histogram fitting to extract lifetimes from photon arrival histograms via least-squares fitting;[37−39] photon-by-photon likelihood maximization;[40−42] construction of Bayesian posteriors over lifetimes warranted by the data;[43−49] and classic deconvolution methods.[50−52]

In spite of this progress in FLIM data analysis, only one such technique that we developed does not assume a number of fluorophore species *a priori* while propagating error over the number of species warranted by the data.[53] Even so, we limited ourselves to a single pixel (i.e., single illuminated confocal spot) and therefore did not leverage spatial correlations across pixels to extract high-resolution lifetime maps required to smoothly and quantitatively interpolate lifetime maps between and below pixel areas.

While heuristics exist to deduce the number of fluorophore species,[54] these do not model the physics properly to propagate errors/information from all of the sources and rely on data preprocessing, which fundamentally limits the ability of these methods to separate close lifetimes. Indeed, other existing techniques, except the one above, require prior knowledge of the number of fluorophore species[34−41,43−47,55] while, when analyzing images, analyze them in a spot-by-spot (spatially decorrelated) manner.[30,31,39,44−46,53]

Ideally, we must therefore avoid data preprocessing (such as histogram fitting by TCSPC) to learn spatial lifetime maps of each species simultaneously deduced (as opposed to specifying the number of species by hand). To be clear, even hypothesized single fluorophore species specified by hand may cause problems as apparent single species may further split into multiple species on the basis of the local chemical

environments to which they are exposed within a cell.[56,57] To further motivate why learning the number of species from the data is critical, we highlight that multiple species may have similar lifetimes and exist in spatially overlapping regions, further underscoring the importance of propagating error and accounting for spatial correlation across pixels while satisfying the underlying Poisson emission statistics.

To compensate for the loss of information in data preprocessing, multiple methods therefore require large photon budgets that otherwise carry the risk of specimen photodamage.[35,39,46] Here, by contrast, our objective is to simultaneously deduce: (1) the number of fluorophore species present within a given FLIM data set and (2) learning absolute lifetime maps with subnanosecond temporal resolution, i.e., distinguishing lifetimes with subnanosecond difference, and interpolating lifetime maps below subpixel for each species determined in the first point. We do so by leveraging the spatial correlations between pixels and information within pulses (termed empty pulses) that do not lead to any photon observation. We develop a framework within the Bayesian paradigm precisely to propagate all sources of errors over items 1−2 above.

Yet, since the number of fluorophore species and their associated maps are unknown, we must operate within a Bayesian nonparametric framework illustrated in Figure 1. As we consider all possible lifetimes in addition to all possible maps that may explain the data, our framework is, in fact, doubly nonparametric.

To be precise, we invoke the beta-Bernoulli process prior[58−61] over each candidate species. That is, we associate a binary weight, $b \in \{0, 1\}$, to each map where nonzero weights are ascribed to those lifetime maps warranted by the

data. As such, the number of lifetime maps present in a given data set are enumerated as the number of nonzero weights, Figure 1c. Next, as our goal is to determine what spatial maps for each species determined are warranted by the data of all possible candidate lifetime maps (of a nominally infinite number), we invoke Gaussian process (GP) priors.[61−65] This is critical in allowing us to learn continuous lifetime maps smoothly over large spatial regions,[55] rather than relying on concatenated pixel-wise maps derived from independent pixel analyses. As we will see, a value for the lifetime map can be deduced at any point in physical space of the infinitely dense points in the two-dimensional focus plane, even below a pixel value with correctly propagated uncertainty.

In the following, we show that our Bayesian nonparametric FLIM (BNP-FLIM) framework learns the number of species (with corresponding lifetimes with subnanosecond resolution) while interpolating lifetime maps below pixel size using limited FLIM data from experiments described above.

■ METHODS

In this section, we briefly discuss the mathematical formulation for our BNP-FLIM framework and the synthetic data generation procedure. Full model details developed herein can be found in the Supporting Information.

Model Formulation. BNP-FLIM starts from stochastic photon arrivals, designated by $\overline{\overline{\Delta t}}$, where the double overbar represents the entire set of photons from all pixels. The stochasticity in the data is introduced from the inherent random nature of the photon emission and detection processes. The stochastic nature of the arrival times motivates our probabilistic analysis framework.

Our framework starts from the likelihood, i.e., probability of the data given model

$$P(\overline{\overline{W}}, \overline{\overline{\Delta t}}|\vartheta) = \prod_i \prod_k P(W_k^i|\vartheta)P(\Delta t_k^i|\vartheta) \tag{1}$$

where $\overline{\overline{W}}$ represents a set of binary random variables W_k^i for the kth pulse in the ith pixel indicating whether the pulse leads to a photon detection or not (empty or nonempty pulse); see Figure S9. Also, ϑ collects the set of parameters we wish to learn including: lifetime values (τ_m for all species), lifetime maps (Λ_m), the means of the GPs (ν_m) on which we place a hyperprior (a prior over another prior parameters), and the binary weights (b_m) associated with each fluorophore species. As we will see, the binary weights are Bernoulli random variables realized to unity for existing species warranted by the data and zero otherwise. Here, m indexes the number of species and runs from 1: M. In Bayesian nonparametrics, we consider $M \rightarrow \infty$ *a priori* and determine which lifetimes ultimately are warranted by the data; See Supplementary Table 1 and Figure S10 for a detailed summary of the notation.

Furthermore, $P(W_k^i|\vartheta)$ and $P(\Delta t_k^i|\vartheta)$, respectively, denote the likelihood of an individual pulse and photon arrival time. In the following, we describe each of these likelihood parts in more detail.

We start by describing the likelihood for the binary observation W_k^i, $P(W_k^i|\vartheta)$. This parameter follows a Bernoulli distribution with success probability of observing a photon of 1 − π_0^i leading to the following likelihood

$$P(W_k^i|\theta) = \text{Bernoulli}(W_k^i; 1 - \pi_0^i) \tag{2}$$

where π_0^i denotes the probability of observing no photons from the ith pixel. The explicit form for π_0^i is derived shortly.

The next observation coincides with the photon arrival times from nonempty pulses, Δt_k^i, which can originate from any of the fluorophore species present in input data. To obtain the portion of the likelihood for the photon arrival times, $P(\Delta t_k^i|\vartheta)$, we need to take into account the IRF and sum over all possible events leading to a photon observation, including all N previous pulses that could have excited the fluorophore and all M fluorophore species that might have led to this photon. This returns

$$P(\Delta t_k^i|\vartheta) = \left[\sum_{m=1}^{M} \pi_m^i \sum_{n=0}^{N} \frac{\lambda_m}{2}\exp\left(\frac{\lambda_m}{2}(2(\tau_{\text{IRF}} - \Delta t_k^i - nT) + \lambda_m\sigma_{\text{IRF}}^2)\right)\right.$$
$$\left. \times \text{erfc}\left(\frac{\tau_{\text{IRF}} - \Delta t_k^i - \text{nT} + \lambda_m\sigma_{\text{IRF}}^2}{\sigma_{\text{IRF}}\sqrt{2}}\right)\right] \tag{3}$$

where π_m^i gives the probability of detecting a photon from the mth fluorophore species in the ith pixel. Here, τ_{IRF}, σ_{IRF}, T, and λ_m, respectively, denote the IRF offset, IRF variance, interpulse time (precalibrated parameters), and inverse of the lifetime (1/τ_m). Derivation details are provided in Supplementary Note 1.1 and Figure S9.

After introducing likelihoods in broad terms, we now turn our attention to the probabilities π_m^i and π_0^i appearing within our likelihoods. These quantities are directly related to the lifetime maps as follows[55]

$$\pi_m^i = (1 - P_{0m}^i) \prod_{r \neq m} P_{0r}^i \tag{4}$$

where P_{0m} denotes the probability of no photon observation from the mth species given by[55]

$$P_{0m}^i = \exp\left[-b_m \int \Lambda_m(X)\text{PSF}(\xi^i; X)dX\right] \tag{5}$$

where PSF, ξ_i, and X, respectively, denote the confocal point spread function, the center of the ith pixel corresponding to the center of PSF, and three-dimensional spatial coordinates. Furthermore, $\Lambda_m(X)$ is set to $\mu_m(X)\rho_m(X)$, where $\mu_m(X)$ denotes the excitation probability (related to photon absorption probability and quantum yield) of a fluorophore of type m during a single pulse and $\rho_m(X)$ denotes the concentration of fluorophores.[55] Moreover, for lifetime maps with zero weights ($b_m = 0$), eq 5 reduces to unity leading to zero probability of observing photons from the corresponding species.

Here, we learn absolute lifetime maps by leveraging the information carried by pulses, leading to no photon observation, termed empty pulses. This is in contrast to previous FLIM analyses[43−48,53] that only take into account the set of observed photons from different species in pixel i, and learn the ratio of lifetime maps by calculating probabilities of photon observations from different species, π_m^i.

The probability of observing no photon from the ith pixel is given by the product of probabilities of no photon observation from all species

$$\pi_0^i = \prod_{m=1}^{M} P_{0m}^i \tag{6}$$

where P_{0m}^i is the probability of no photon detection from species m. Considering empty pulses, the sum of these probabilities is naturally unity

$$\pi_0^i + \sum_{m=1}^{M} \pi_m^i \simeq 1 \tag{7}$$

under the assumption that there is no more than a single detected photon per pulse.[55] To build further intuition, as a sanity check, we can verify that removing the contribution from empty pulses (π_0^i) from the above equation results in a sum no longer equal to unity. As such, methods ignoring empty pulses rescale probabilities π_m^i to make them resume to unity and, as a result, learn only rescaled values, i.e., photon ratios, rather than the absolute values.

Model Inference. In the previous section, we described our likelihood model. In this section, we use the derived likelihood to construct the posterior of all of the unknowns, which is proportional to the product of the likelihood and priors on the unknown parameters

$$P(\vartheta|\overline{\overline{\Delta t}}, \overline{W}) \propto P(\overline{\overline{\Delta t}}, \overline{W}|\vartheta)P(\vartheta) \tag{8}$$

The most notable priors in the BNP-FLIM framework are the nonparametric GP priors on the set of lifetime maps and the nonparametric beta-Bernoulli process priors[58−60] on the binary weights

$$\Lambda_m \sim \mathrm{GP}(\nu_m, \mathbf{K}) \tag{9}$$

$$q_m \sim \mathrm{beta}(A_q, B_q) \tag{10}$$

$$b_m \sim \mathrm{Bernoulli}(q_m) \tag{11}$$

where ν_m and $\mathbf{K}$ are, respectively, the GP prior mean and the covariance matrix, and A_q, B_q are beta-Bernoulli process hyperparameters. The remaining, standard priors are discussed in Supplementary Note 1−2.

The full joint posterior eq 8 does not attain an analytic form from which we can sample all variables directly. Thus, in developing the BNP-FLIM framework, we propose a numerical means by which to sample our posterior to draw inferences about unknown parameters using Markov Chain Monte Carlo techniques[60,66−74] (see details in Supplementary Note 2). Furthermore, while nominally the number of fluorophore species are infinite $(M \rightarrow \infty)$ within the nonparametric paradigm, here we instead follow refs 58−60 and set a large upper limit on the number of species (M) in lieu of infinity and ensure ourselves that these results are independent in of this limit.

More specifically, our MCMC chain is structured in such a way as to sweep through the entire set of parameters (i.e., via Gibbs sampling) at every iteration by independently drawing samples from each parameter's conditional posterior; see Supporting Information Note 2. To do so, we sweep the parameter set as follows (the order in which the parameters are swept is arbitrary):

- lifetime maps, Λ_m—these can be sampled either using the conceptually simpler Metropolis−Hastings (MH)[61,75,76] or the more efficient elliptical slice sampling.[77] We opt for the latter. Either method of

sampling for lifetime maps is required as the likelihood derived in eqs 1−3 is not conjugate to the GP prior.

- mean of GP priors, ν_m—we use MH to sample the GP means, ν_m, due to lack of conjugacy between prior and likelihood;

- lifetimes, τ_m—we sample the lifetimes, τ_m, again using MH due to lack of conjugacy;

- the binary weights, b_m—we update the binary weights, b_m, by modifying a subset of b_m by randomly selecting a subset and directly sampling from the posterior for that subset (see Supplementary Note 2).

In the end, the chain of samples drawn is used for subsequent numerical analysis.

Synthetic Data Generation. Before we describe our results, we illustrate our procedure for simulating data. To be more precise, we explain the data simulation procedure for a single pixel (ith pixel) in order to later simulate all multipixel FLIM data used across this study. To do so, we assume a set of $\mathcal{M}$ lifetime maps corresponding to $\mathcal{M}$ fluorophore species (typically $\mathcal{M}$ is much smaller than the truncated M we use in the Methods section to approximate the beta-Bernoulli process prior). Next, we use lifetime maps to simulate data in the ith pixel by (1) sampling W_k^i to determine whether the kth pulse results in a photon or not (i.e., is empty or nonempty pulse) from a Bernoulli distribution similar to eq 2; (2) sampling the fluorophore species, $m \in \{1, ..., \mathcal{M}\}$, giving rise to the detected photons, for nonempty pulses, from a categorical distribution, i.e., a discrete distribution with more than two options, with probabilities $\pi_{1:\mathcal{M}}^i$ given by eqs 4 and 5; (3) sampling the period spent in the excited state by the fluorophore, $\Delta t_{\mathrm{ext},k}^i$, from an exponential distribution with lifetime τ_m; (4) sampling the IRF time, $\Delta t_{\mathrm{IRF},k}^i$, from a Gaussian distribution and adding it to the time spent in the excited state by the fluorophore; and finally (5) deal with cases where the sum of both those times generated in steps 3 and 4 exceeds the interpulse time T.

To elaborate briefly on step 5, since the photon arrival times are recorded with respect to the immediately preceding pulse (sometimes termed the "microtime" in FLIM), they are always smaller than the interpulse window. As such, to allow for the possibility that some arrival times may exceed the interpulse window (especially when the excited state lifetime is on par with the interpulse window), we need to introduce a third term subtracting integer interpulse windows from the generated arrival times

$$\Delta t_k^i = \Delta t_{\mathrm{ext},k}^i + \Delta t_{\mathrm{IRF},k}^i - T \left\lfloor \frac{\Delta t_{\mathrm{ext},k}^i + \Delta t_{\mathrm{IRF},k}^i}{T} \right\rfloor \tag{12}$$

where the bracket returns the integer part of its content. We note, as a sanity check, that if an arrival time is smaller than the interpulse window, the third term is zero. Moreover, the parameters used in the simulations are inspired by values from the experimental data used later. That is, we sample IRF times from a Gaussian distribution with mean and standard deviation of 12.20 and 0.8 ns, respectively. Furthermore, we use interpulse time and pixel size of $T = 12.8$ ns and 0.39 μm and assume a Gaussian PSF (see eq 5) with $\sigma_{xy} = 0.54$ μm and $\sigma_z = 1.56$ μm. Other parameter values used in the analyses are provided in Supplementary Table 2.
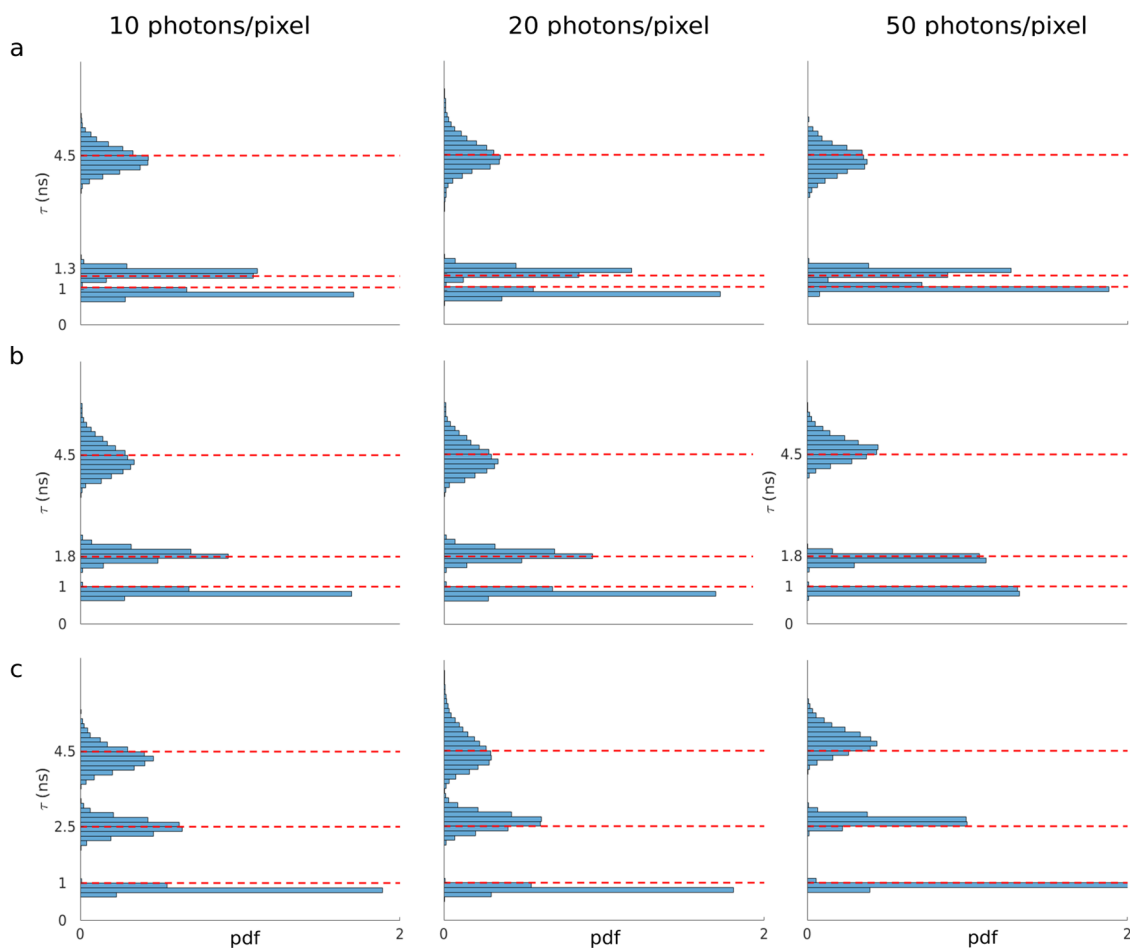
Figure 2. BNP-FLIM robustness with respect to photon counts per pixel and lifetime differences. Three overlapping lifetime maps with different lifetimes were generated over a region of 5 × 20 pixels and processed by the BNP-FLIM framework. There are two fixed lifetimes of 1 and 4.5 ns in all simulated data, while we varied the third lifetimes to obtain lifetime differences of (a) 0.3 ns; (b) 0.8 ns, and (c) 1.5 ns. Histograms show the resulting lifetime samples from the posterior of the BNP-FLIM framework, and the red dashed lines denote ground truth values.
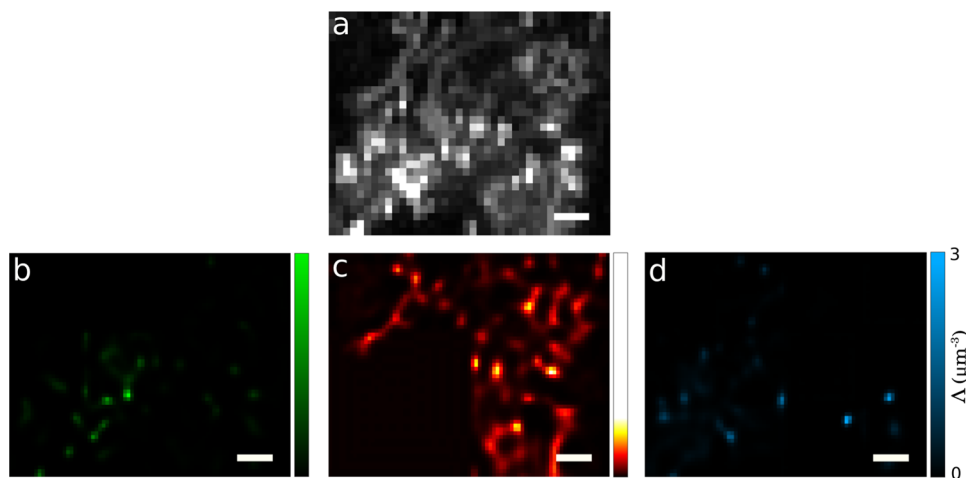

Figure 3. *In vivo* data set containing three fluorophore species. (a) Data acquired by scanning the sample over area of 30 × 40 pixel. The sample is simultaneously labeled with three fluorophore species of pHrodo with a lifetime of 0.8 ns staining lysosomes, TMRM with a lifetime of 2.8 ns staining mitochondria, and Lyso-Red with a lifetime of 4.5 ns staining endosomes. This resulted in three lifetime maps interpolated below pixel size (1/2 pixel). (b) Lifetime maps corresponding to a lifetime of 0.8 ns; (c) lifetime map corresponding to a lifetime of 2.8 ns; and (d) lifetime map corresponding to a lifetime of 4.5 ns. Scale bars are 2 μm. The color bar cutoffs in (d) apply to (b) and (c) as well.
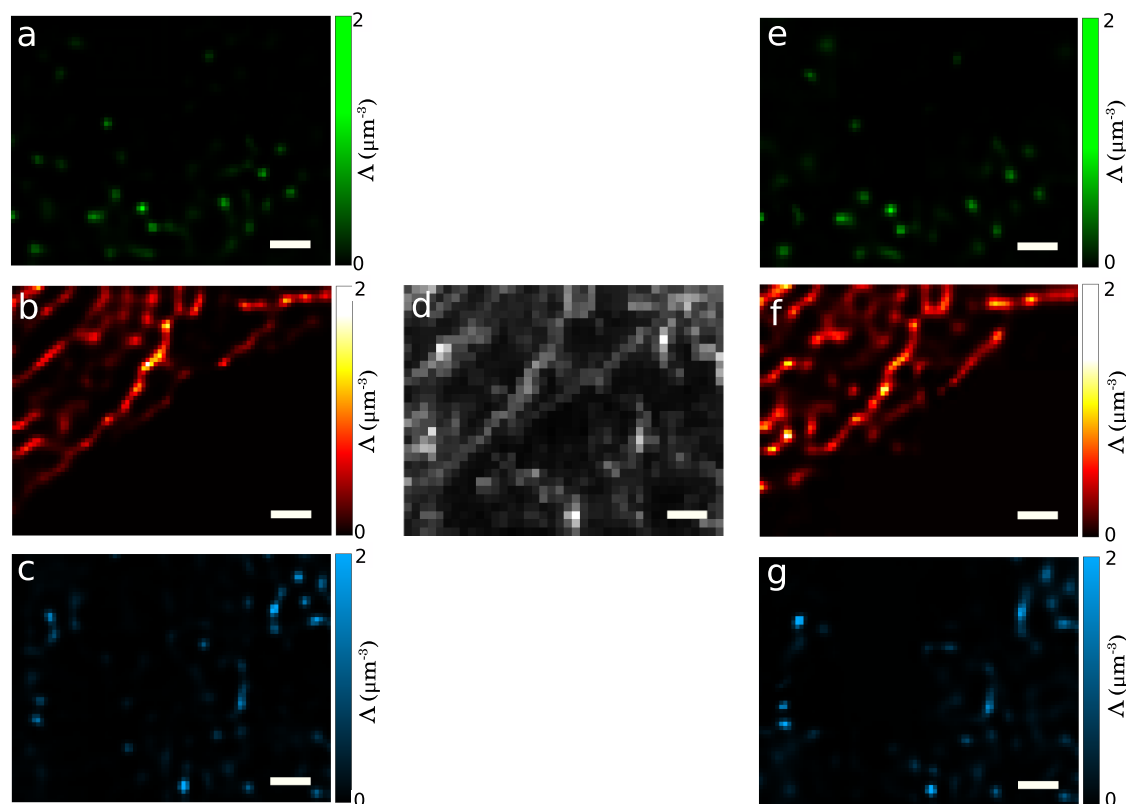
Figure 4. In order to test our method on realistic distributions of fluorophores, we consider *in vivo* FLIM data composed, as a test of our method, by mixing three single-species lifetime maps into one. That is, we first analyze three data sets each containing a single species to produce the "ground truth" maps seen in (a)−(c). More concretely: (a) the "ground truth" lifetime map (green) for pHrodo with a lifetime of 0.8 ns; (b) the "ground truth" lifetime map (red) for TMRM with a lifetime of 2.8 ns; and (c) the "ground truth" lifetime map (blue) for Lyso-red with a lifetime of 4.5 ns. Now, we combine our three original data sets to produce (d). Next, we apply BNP-FLIM to learn the number of species and their maps that we show in (e)−(g) and can now compare, respectively, with (a)−(c). Lifetime maps in (a)−(c) and (e)−(g) are reported with a pixel size equal to 1/2 the pixel size of (d). Scale bars are 2 μm. The agreement between (a)−(c) and (e)−(g) is discussed in the text.

■ RESULTS

The overarching aim of our BNP-FLIM framework described above is to develop the posterior and sample from it to learn the number of fluorophore species, i.e., number of nonzero binary weights b_m coinciding with the number of species, warranted by the data, the corresponding lifetimes, τ_m, and lifetime maps, designated by $\Lambda_{1:M}$, using a set of input photon arrival times $\overline{\overline{\Delta t}}$ and pulse occupancies $\overline{\overline{W}}$; see Supplementary Table 1 for a description of the parameters.

To do so, the BNP-FLIM framework draws numerical samples from our joint posterior for these parameters, as illustrated in the Methods section. Our results as histograms over numerical samples drawn from our Monte Carlo sampling scheme. Uncertainties naturally follow from the widths of our histograms over each quantity of interest, reflecting a numerical approximation to our true marginal posteriors.

In this section, we use a range of synthetic and experimental data to benchmark our framework against different lifetime maps including: (1) simple, smoothly varying, homogeneous lifetime maps (see Figures 2 and S1) and (2) more difficult lifetime maps with heterogeneous features similar to those present in experimental samples (see Figures 3−5 and S2−S7). In addition, employing simulated data with smoothly varying lifetime maps, we further evaluate our BNP-FLIM framework's performance over a wide range of lifetimes, lifetime differences, and photon counts (see Figure 2). Finally, we focus our discussion on a single pixel to determine the number of

photons required to assess the number of species and their lifetimes as a function of decreasing interpulse times for the challenging case of similar lifetimes; see Figures 6 and S8.

Robustness with respect to Photon Counts and Lifetime Resolution. Here, we start by considering smoothly varying lifetime maps (before turning to more complex maps in the next section). We use these maps to benchmark our BNP-FLIM framework against a range of lifetimes, lifetime differences, and photon counts. To do so, we use three synthetic maps corresponding to three different lifetimes over an area of 5 × 20 pixels. We use the combination of these maps to generate data sets with 10, 20, and 50 photons per pixel shown in the first, second, and third columns in Figure 2, respectively. Row a in Figure 2 shows the resulting lifetime histograms where two of the lifetimes differ by only 0.3 ns representing a challenging case with subnanosecond lifetime differences. Here, the BNP-FLIM framework correctly assigns nonzero binary weights to three lifetime maps and learns the corresponding lifetimes accomplishing subnanosecond lifetime resolution even with 10 photons per pixel and 1000 photons in total. We also note that by increasing the photon counts to 20 and 50 photons per pixel, the histograms' widths tend to decrease, signifying smaller uncertainties. Next, as we move to larger differences in lifetime in rows b and c, we expect to observe sharper histograms due to less uncertainty. However, the histograms do not exhibit such behavior due to posterior broadening for larger lifetimes. This is because fluorophore
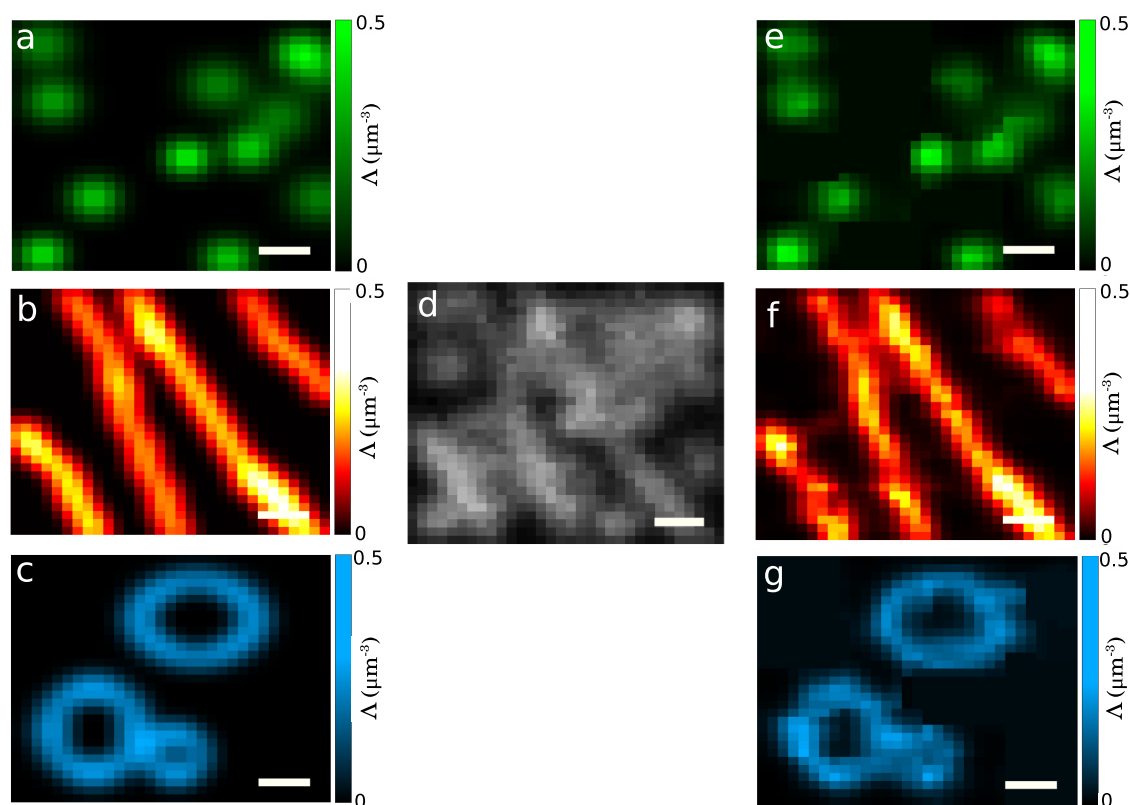
Figure 5. Simulated FLIM data generated from a mixture of three lifetime maps. (a) Ground truth map simulated with lifetime of 1 ns. (b) Ground truth map simulated with lifetime of 2.5 ns. (c) Ground truth map simulated with lifetime of 4.5 ns. (d) Data generated using a mixture of lifetime maps in (a)−(c). This data was processed using the BNP-FLIM framework resulting again in three nonzero binary weights and corresponding lifetime maps with lifetimes of (e) 1 ns, (f) 2.5 ns, and (g) 4.5 ns. Scale bars are 2 μm.

species with larger lifetimes are more likely to stay excited longer than an interpulse period, leading to more photons detected in one or more pulses following the one inducing fluorophore excitation. Despite this, we still see histogram sharpening with more photons per pixel from left to right for each row. Further, cross sections of lifetime maps corresponding to these lifetimes are represented in Figure S1. Here, although we are able to achieve subnanosecond lifetime resolution by using photons from across the entire region, the spatial lifetime maps are learned using only photons from specific areas, i.e., pixels, which can result in poorer uncertainties in the estimated maps, particularly for the case with 10 photons per pixel, compared to the inferred lifetimes.

Heterogeneous Simulated and *In Vivo* Lifetime Maps. Here, we challenge our BNP-FLIM framework using lifetime maps with more complex features. To do so, we use data including: *in vivo* data acquired by labeling three different subcellular structures using different fluorophore species in Figure 3; a mixed image composed of single-species *in vivo* data in Figures 4 and S3−S6; and synthetic data generated from heterogeneous lifetime maps mimicking ones recovered *in vivo* (see Figure 5).

Here, we start by assessing the performance of the BNP-FLIM framework using data acquired by scanning an area of 30 × 40 pixels of an *in vivo* sample stained by three fluorophore species: pHrodo with a lifetime of 0.8 ns which binds to lysosomes; TMRM with a lifetime of 2.8 ns which binds to mitochondria; Lyso-red with a lifetime of 4.5 which binds to endosomes (see Figure 3a). The BNP-FLIM framework correctly learns the number of lifetimes present in the data

with the corresponding lifetimes shown in Figure S2. For the lifetimes, the average difference of the ground truths and the histogram peaks is approximately 0.2 ns (where the ground truth in the SI is taken to originate from a very large number of photons using the phasor method[30]). Moreover, Figure 3 depicts lifetime maps interpolated below pixel size (1/2 pixel) corresponding to pHrodo, TMRM, and Lyso-Red shown in green, red, and blue, respectively. However, in this case, we cannot benchmark BNP-FLIM using lifetime maps due to the lack of ground truth maps. For this reason, we use a hybrid data set consisting of three single species *in vivo* data and synthetic data, described below.

We begin by first describing each single-species lifetime map within the hybrid *in vivo* data set. These data sets were acquired by scanning 30 × 40 pixel regions of three different samples (see Figure S3a−c). Each sample contained one of the fluorophore species: pHrodo, TMRM, and Lyso-red. Figure 4a−c, respectively, represents the lifetime maps learned from the raw data shown in Figure S3 reporting lifetime maps at 1/2 the pixel for pHrodo (green), TMRM (red), and Lyso-Red (blue). These lifetime maps are obtained by analyzing each individual data set using the BNP-FLIM framework (also see Figure S3d−f). Moreover, Figure S4 shows the resulting lifetime histograms where the histogram peaks differ from the ground truth by less than 0.07 ns on average (where ground truth lifetimes were again taken to be values found using phasor method).

We now evaluate the performance of our framework by combining all three data sets. The ground truth is now taken as
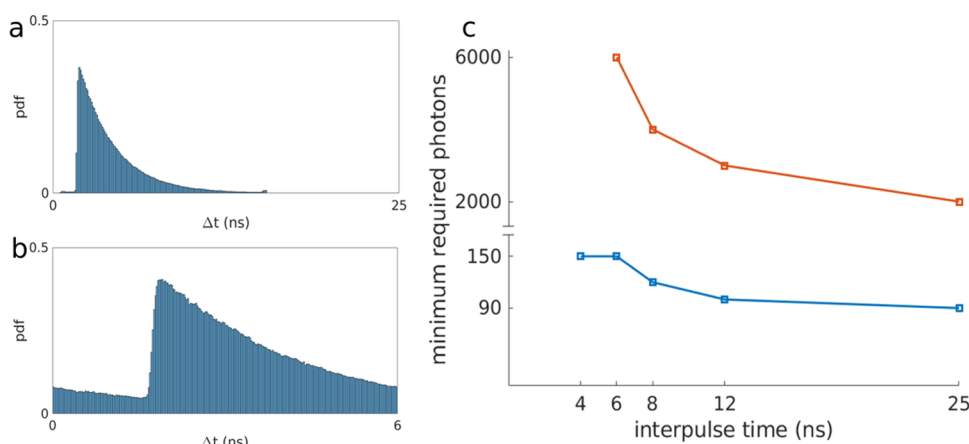
Figure 6. Required a minimum number of photons in order to infer the number of fluorophore species and corresponding lifetimes with respect to the interpulse time window (T). As an example only, we present histograms of experimental photon arrival times for one species (with lifetimes of 2.4 ns) under two different interpulse windows: (a) has $T = 25$ ns and (b) has $T = 6$ ns. The data sets used here were originally collected with an interpulse time of 25 ns, and data sets with smaller interpulse times are generated from the raw data as detailed in the text. In (c), we show the smallest photon counts required for our BNP-FLIM framework to begin deducing the exact number of lifetimes and the corresponding lifetimes (with less than ≈18% average error). The blue curve represents results for data sets acquired using a single dye of Rho6G with a lifetime of 2.4 ns. The red curve represents results for data sets obtained using two dyes of Rho6G and RhodB with lifetimes of 2.4 and 1.4 ns, respectively. The two lifetimes are only 1 ns apart and are collected over a single pixel. Here, pdf denotes the probability density function obtained by normalizing the area under the histogram to one.

the lifetime maps shown in Figure 4a−c that were obtained by analyzing the single-species data sets.

Our BNP-FLIM framework correctly identified three species (as the *maximum a posteriori* estimate) and their coinciding lifetime maps are shown in Figure 4e−g with the learned maps interpolated below pixel size (1/2 pixel) for pHrodo (green), TMRM (red) and Lyso-Red (blue). To quantitatively compare the resulting maps in Figure 4a−c and the ground truth maps (Figure 4e−g), we calculated their absolute relative differences given by $|\Delta\Lambda|/\max(\Lambda_{\text{true}})$, where Λ_{true} denotes the ground truth map. The error maps are shown in Figure S5 with the mean errors of ≈3%, ≈8%, and ≈6% for pHrodo, TMRM, and Lyso-Red, respectively. Moreover, the resulting histograms of the number of nonzero binary weights and the corresponding lifetimes are shown in Figure S6. For lifetimes, the average difference between ground truth values and histogram peaks is approximately 0.12 ns.

After assessing the performance of our BNP-FLIM framework using *in vivo* data, we continue to benchmark our framework using synthetic FLIM data containing three complex lifetime maps (see Figure 5a−c) similar to those in experimental data with lifetimes of 1, 2.5, and 4.5 ns, generated over an area of 32 × 32 pixels (see Figure 5d). We used our BNP-FLIM framework to analyze this data. The resulting lifetime maps are shown in Figure 5e−g with average absolute relative differences of ≈5%, ≈ 8%, and ≈5%, respectively. Moreover, the histograms of the number of nonzero binary weights warranted by the data and the corresponding lifetimes are given in Figure S7. Here, the histogram in the number of species has peaks at the true value of 3 and peaks of the lifetime histograms differ from the ground truths by less than 0.08 ns on average (see Figure S7).

Finally, we narrow our focus to a single pixel to investigate the effect of interpulse time (T) on the photon counts required to deduce the number of fluorophore species as well as their lifetimes for *in vitro* (see Figure 6) and simulated data (see Figure S8). Experimental data sets were acquired using Rho6G and a combination of RhodB and Rho6G with lifetimes only 1

ns apart, namely, 1.4 and 2.4 ns, respectively. These data sets were originally collected with $T = 25$ ns.[53] From these data, it is possible to generate arrival times with smaller interpulse times using $\Delta t = \Delta t - T \lfloor \Delta t/T \rfloor$. Here, the bracket gives the integer part of its content. Our framework deduces the single lifetimes using only 90 and 150 arrival times acquired experimentally for $T = 25$ ns (under the reasonable assumption that no dye can statistically remain excited longer than the interpulse time given our finite sample) and $T = 4$ ns (where many dyes remain excited for multiple interpulse times following the pulse giving rise to the original excitation), respectively. Moreover, for experimental data sets with two species, we can distinguish the number of lifetimes and their associated lifetime values using approximately 2000 and 6000 photons for $T = 25$ ns and $T = 6$ ns; see Figure 6. In both cases, shorter interpulse times require more photons as shorter interpulse times result in photon emissions of multiple pulses following excitation giving rise to a less informative posterior. In the case of $T < 6$ ns (red curve in Figure 6c), our BNP-FLIM framework could not distinguish the two lifetimes due to the abundance of photon emissions following multiple laser pulses.

As a further test beyond the *in vitro* data analyzed, the simulated data sets were generated using either one or two lifetimes of 1.4 and 2.4 ns (similar to the experimental data in Figure 6) and interpulse times of 25, 12, 8, 6 and 4 ns over a single pixel; see Figure S8. BNP-FLIM started deducing the correct lifetime for data sets containing a single lifetime using approximately 20 photons for $T = 25$ ns and 70 photons for $T = 4$ ns; see Figure S8. For cases with two species, our framework inferred the correct number of lifetimes for $T = 25$ ns using 800 photons and 3000 photons for $T = 6$ ns. Finally, we add that in contrast to Figure 2, these data represent a more difficult case as all species are overlapping in a single pixel (no spatial information), while for Figure 2, we can leverage spatial separation to discriminate between fluorophore species and their associated lifetime values. As such, we need more photons here than we do in Figure 2.

EXPERIMENTAL METHODS

Experimental data were acquired on an ISS-Alba confocal microscope. Excitation was provided by a 780 nm 2-photon laser pulsed at 80 MHz (Calmar Laser). Emission was collected by an avalanche photodiode (Excelitas Technologies) and an ISS A320 Fast FLIM unit for lifetime determination. A 760 short-pass dichroic was used to split the excitation and emission light; no additional emission filter was used. Images were collected with a 16 μs pixel dwell time with an image size of 256 × 256 pixels and a 0.39 μm pixel size, accumulating 7−9 frames for each data set. After each experiment, the images were preprocessed by extracting individual photons and constructing a list of arrival times for each photon, both in reference to the start of the measurement and to the previous laser pulse. MDA-MB-231 cells were seeded in a glass-bottom 8-well plate (Ibidi GmbH) previously coated with 2 μg/mL Fibronectin in Dulbecco's phosphate buffer solution (DPBS) without Ca, Mg, Phenol Red (GenClone, Genesee). Cells were stained with 50 μg/mL pHrodo Green Dextran, 10,000 MW, 100 nM TMRM, and 50 nM LysoTracker Deep Red (Invitrogen) for 4 h and subsequently imaged.

CONCLUSIONS

Fluorescence lifetime imaging techniques allow us to probe life within complex subcellular environments. In particular, these techniques have been employed to detect changes in cellular metabolism due to cancer metastasis[78−80] whose ensuing metabolic shift is detected by monitoring varying levels of free and bound NADH within breast tissue cells.[78] Moreover, quantitative interpretation of FLIM data remains limited by fundamentally unknown numbers of fluorophore species to which to fit the data and high photon counts required to determine lifetimes separated by small differences, such as difficulty in discriminating lifetimes with subnanosecond differences. Further, the spatial resolution of raw FLIM data is limited to the PSF size given an optimal pixel size, namely, half of the PSF size according to the Nyquist criterion. While quantitative FLIM methods can resolve features beyond the PSF size when deconvolving data, these approaches remain limited to the pixel size (the distance between scanned lines) in reconstructing lifetime maps. Here, using BNP-FLIM, we can provide smooth lifetime maps by interpolating beyond the pixel size leveraging all spatial correlations across pixels; see Figure 3 and 4. Addressing these issues requires a framework leveraging all spatial information and the known physics of the problem by incorporating it directly into the likelihood. This physics includes Poisson photon emission statistics and spatial correlations across pixels as well as all existing noise sources, e.g., IRF, to simultaneously learn the number of species and associated maps.

Of importance here is the fact that simulated data can be generated at will to test the number of photons required as lifetimes of different species become more similar, their distribution overlaps more closely in space (e.g., Figure 2 versus Figure S8), and the number of species rises or interpulse times shrink (e.g., Figure S8). In principle, there is no theoretical limit imposed on how similar lifetimes can be given infinite photons, though there may be practical limits pertaining to the breath of the IRF and photodamage induced on the sample required in the collection of large photon numbers. We also argue that the number of photons we use to achieve subnanosecond lifetime resolution from this exercise

essentially defines a lower bound as BNP-FLIM introduces minimal data preprocessing. Any form of preprocessing, e.g., arrival times binning,[37−39] naturally results in information loss and thus requires more photons in deducing lifetimes or their spatial distribution.[49]

Due to our choice of Monte Carlo samplers in BNP-FLIM, the computational cost scales linearly with the number of pixels and photon counts. Moreover, the computational cost also depends on the type of data analyzed. For instance, more challenging data sets, such as data sets containing lifetime maps with more complex features or multiple lifetime maps (where background could be considered yet another species), complicate the posterior's shape. This necessarily requires us to draw more samples from the posterior and therefore introduces a higher computational cost. For example, it took 2 days of computer wall time (not active human work) to analyze the single species *in vivo* data sets shown in Figure S3, while it took about a week of wall time to analyze the *in vivo* data set containing three lifetime maps shown in Figure 4d on a regular desktop machine with AMD Ryzen 9 3900X 3.8 GHz CPU and 64 GB RAM.

Although we assumed a Gaussian IRF for simplicity while retaining sufficient accuracy, the BNP-FLIM framework is also capable of accommodating any type of IRF by simply modifying eq 3 at no additional computational cost. Moreover, here, we assumed that parameters of the IRF distribution, e.g., offset and variance, can be precalibrated. However, our inverse strategy can be generalized to learn these parameters along with the rest of the unknowns by adding appropriate priors on these parameters. Furthermore, for species present at low concentrations, the probability of no excitation, appearing in eq 5, can be approximated by the first two terms of their Taylor expansion, leading to simpler expressions and reduced computational complexity.

ASSOCIATED CONTENT

Data Availability Statement

The experimental data used in this work are available upon reasonable request from the corresponding author. The software package is available at https://github.com/MohamadFazel/BNP2-FLIM.

ⓢ Supporting Information

The Supporting Information is available free of charge at https://pubs.acs.org/doi/10.1021/acsphotonics.3c00595.

> Cross sections of lifetime maps corresponding to Figure 2 (Figure S1); histograms of lifetime and number of found species corresponding to Figure 3 (Figure S2); deduced lifetime maps and lifetime histograms of data with single species (Figures S3 and S4); error maps and histograms of found lifetimes and species numbers corresponding to Figure 4 (Figure S5 and S6); histograms of found lifetimes and species numbers corresponding to Figure 5 (Figure S7); results similar to Figure 6 using synthetic data (Figure S8); details of the mathematical framework including the likelihood and posterior derivations (Supplementary Note 1); and inference framework and the Monte Carlo sampling procedure for each parameter (Supplementary Note 2) (PDF)

■ AUTHOR INFORMATION

Corresponding Author

Steve Pressé − *Center for Biological Physics and Department of Physics, Arizona State University, Tempe, Arizona 85287, United States; School of Molecular Science, Arizona State University, Tempe, Arizona 85287, United States;* orcid.org/0000-0002-5408-0718; Email: spresse@asu.edu

Authors

Mohamadreza Fazel − *Center for Biological Physics and Department of Physics, Arizona State University, Tempe, Arizona 85287, United States*

Sina Jazani − *Center for Biological Physics and Department of Physics, Arizona State University, Tempe, Arizona 85287, United States*

Lorenzo Scipioni − *Department of Biomedical Engineering, University of California Irvine, Irvine, California 92697, United States; Laboratory of Fluorescence Dynamics, The Henry Samueli School of Engineering, University of California, Irvine, California 92697, United States*

Alexander Vallmitjana − *Department of Biomedical Engineering, University of California Irvine, Irvine, California 92697, United States; Laboratory of Fluorescence Dynamics, The Henry Samueli School of Engineering, University of California, Irvine, California 92697, United States;* orcid.org/0000-0002-7149-9385

Songning Zhu − *Department of Biomedical Engineering, University of California Irvine, Irvine, California 92697, United States; Laboratory of Fluorescence Dynamics, The Henry Samueli School of Engineering, University of California, Irvine, California 92697, United States*

Enrico Gratton − *Department of Biomedical Engineering, University of California Irvine, Irvine, California 92697, United States; Laboratory of Fluorescence Dynamics, The Henry Samueli School of Engineering, University of California, Irvine, California 92697, United States;* orcid.org/0000-0002-6450-7391

Michelle A. Digman − *Department of Biomedical Engineering, University of California Irvine, Irvine, California 92697, United States; Laboratory of Fluorescence Dynamics, The Henry Samueli School of Engineering, University of California, Irvine, California 92697, United States*

Complete contact information is available at:
https://pubs.acs.org/10.1021/acsphotonics.3c00595

Notes

The authors declare no competing financial interest.

■ REFERENCES

(1) Suhling, K.; Hirvonen, L. M.; Levitt, J. A.; Chung, P.-H.; Tregidgo, C.; Le Marois, A.; Rusakov, D. A.; Zheng, K.; Ameer-Beg, S.; Poland, S.; et al. Fluorescence lifetime imaging (FLIM): Basic concepts and some recent developments. *Med. Photonics* **2015**, *27*, 3.

(2) Datta, R.; Heaster, T. M.; Sharick, J. T.; Gillette, A. A.; Skala, M. C. Fluorescence lifetime imaging microscopy: fundamentals and advances in instrumentation, analysis, and applications. *J. Biomed. Opt.* **2020**, *25*, No. 1.

(3) Garini, Y.; Young, I. T.; McNamara, G. Spectral imaging: principles and applications. *Cytometry Pt A* **2006**, *69A*, 735.

(4) Huang, B.; Bates, M.; Zhuang, X. Super-resolution fluorescence microscopy. *Annu. Rev. Biochem.* **2009**, *78*, 993.

(5) Fazel, M.; Wester, M. J. Analysis of super-resolution single molecule localization microscopy data: A tutorial. *AIP Adv.* **2022**, *12*, No. 010701.

(6) Lelek, M.; Gyparaki, M. T.; Beliu, G.; Schueder, F.; Griffié, J.; Manley, S.; Jungmann, R.; Sauer, M.; Lakadamyali, M.; Zimmer, C. Single-molecule localization microscopy. *Nat. Rev. Methods Primers* **2021**, *1*, 39.

(7) Fazel, M.; Grussmayer, K. S.; Ferdman, B.; Radenovic, A.; Shechtman, Y.; Enderlein, J.; Pressé, S. Fluorescence Microscopy: a statistics-optics perspective, arXiv:2304.01456. arXiv.org e-Print archive. https://arxiv.org/abs/2304.01456, 2023.

(8) Lidke, D.; Nagy, P.; Barisas, B.; Heintzmann, R.; Post, J. N.; Lidke, K.; Clayton, A.; Arndt-Jovin, D.; Jovin, T. Imaging molecular interactions in cells by dynamic and static fluorescence anisotropy (rFLIM and emFRET). *Biochem. Soc. Trans.* **2003**, *31*, 1020.

(9) Tregidgo, C. L.; Levitt, J. A.; Suhling, K. Effect of refractive index on the fluorescence lifetime of green fluorescent protein. *J. Biomed. Opt.* **2008**, *13*, No. 031218.

(10) Coban, O.; Zanetti-Dominguez, L. C.; Matthews, D. R.; Rolfe, D. J.; Weitsman, G.; Barber, P. R.; Barbeau, J.; Devauges, V.; Kampmeier, F.; Winn, M.; et al. Effect of phosphorylation on EGFR dimer stability probed by single-molecule dynamics and FRET/FLIM. *Biophys. J.* **2015**, *108*, 1013.

(11) Aubret, A.; Pillonnet, A.; Houel, J.; Dujardin, C.; Kulzer, F. CdSe/ZnS quantum dots as sensors for the local refractive index. *Nanoscale* **2016**, *8*, 2317.

(12) Pliss, A.; Prasad, P. N. High resolution mapping of subcellular refractive index by Fluorescence Lifetime Imaging: a next frontier in quantitative cell science? *Methods Appl. Fluoresc.* **2020**, *8*, No. 032001.

(13) Joosen, L.; Hink, M.; Gadella, T., Jr; Goedhart, J. Effect of fixation procedures on the fluorescence lifetimes of Aequorea victoria derived fluorescent proteins. *J. Microsc.* **2014**, *256*, 166.

(14) Inada, N.; Fukuda, N.; Hayashi, T.; Uchiyama, S. Temperature imaging using a cationic linear fluorescent polymeric thermometer and fluorescence lifetime imaging microscopy. *Nat. Protoc.* **2019**, *14*, 1293.

(15) Kalytchuk, S.; Polakova, K.; Wang, Y.; Froning, J. P.; Cepe, K.; Rogach, A. L.; Zboril, R. Carbon dot nanothermometry: intracellular photoluminescence lifetime thermal sensing. *ACS Nano* **2017**, *11*, 1432.

(16) Okabe, K.; Inada, N.; Gota, C.; Harada, Y.; Funatsu, T.; Uchiyama, S. Intracellular temperature mapping with a fluorescent polymeric thermometer and fluorescence lifetime imaging microscopy. *Nat. Commun.* **2012**, *3*, No. 705.

(17) Zhang, H.; Jiang, J.; Gao, P.; Yang, T.; Zhang, K. Y.; Chen, Z.; Liu, S.; Huang, W.; Zhao, Q. Dual-emissive phosphorescent polymer probe for accurate temperature sensing in living cells and zebrafish using ratiometric and phosphorescence lifetime imaging microscopy. *ACS Appl. Mater. Interfaces* **2018**, *10*, No. 17542.

(18) Yin, J.; Peng, M.; Lin, W. Visualization of mitochondrial viscosity in inflammation, fatty liver, and cancer living mice by a robust fluorescent probe. *Anal. Chem.* **2019**, *91*, 8415.

(19) Hao, L.; Li, Z.-W.; Zhang, D.-Y.; He, L.; Liu, W.; Yang, J.; Tan, C.-P.; Ji, L.-N.; Mao, Z.-W. Monitoring mitochondrial viscosity with anticancer phosphorescent Ir (III) complexes via two-photon lifetime imaging. *Chem. Sci.* **2019**, *10*, 1285.

(20) Liu, T.; Campbell, B. T.; Burns, S. P.; Sullivan, J. P.; et al. Temperature-and pressure-sensitive luminescent paints in aerodynamics. *Appl. Mech. Rev.* **1997**, *50*, 227.

(21) Gregory, J. W.; Asai, K.; Kameda, M.; Liu, T.; Sullivan, J. A review of pressure-sensitive paint for high-speed and unsteady aerodynamics. *Proc. Inst. Mech. Eng., Part G* **2008**, *222*, 249.

(22) Lin, H.-J.; Herman, P.; Lakowicz, J. R. Fluorescence lifetime-resolved pH imaging of living cells. *Cytometry* **2003**, *52A*, 77.

(23) Bizzarri, R.; Serresi, M.; Luin, S.; Beltram, F. Green fluorescent protein based pH indicators for in vivo use: a review. *Anal. Bioanal. Chem.* **2009**, *393*, 1107.

(24) Zhu, X.-H.; Lu, M.; Lee, B.-Y.; Ugurbil, K.; Chen, W. In vivo NAD assay reveals the intracellular NAD contents and redox state in healthy human brain and their age dependences. *Proc. Natl. Acad. Sci. U.S.A.* **2015**, *112*, 2876.

(25) Bird, D. K.; Yan, L.; Vrotsos, K. M.; Eliceiri, K. W.; Vaughan, E. M.; Keely, P. J.; White, J. G.; Ramanujam, N. Metabolic mapping of MCF10A human breast cells via multiphoton fluorescence lifetime imaging of the coenzyme NADH. *Cancer Res.* **2005**, *65*, 8766.

(26) Ma, N.; Digman, M. A.; Malacrida, L.; Gratton, E. Measurements of absolute concentrations of NADH in cells using the phasor FLIM method. *Biomed. Opt. Express* **2016**, *7*, 2441.

(27) Frei, M. S.; Tarnawski, M.; Roberti, M. J.; Koch, B.; Hiblot, J.; Johnsson, K. Engineered HaloTag variants for fluorescence lifetime multiplexing. *Nat. Methods* **2022**, *19*, 65.

(28) Kumar, S.; Alibhai, D.; Margineanu, A.; Laine, R.; Kennedy, G.; McGinty, J.; Warren, S.; Kelly, D.; Alexandrov, Y.; Munro, I.; et al. FLIM FRET Technology for Drug Discovery: Automated Multiwell-Plate High-Content Analysis, Multiplexed Readouts and Application in Situ. *ChemPhysChem* **2011**, *12*, 609.

(29) Conway, J. R. W.; Carragher, N. O.; Timpson, P. Developments in preclinical cancer imaging: innovating the discovery of therapeutics. *Nat. Rev. Cancer* **2014**, *14*, 314.

(30) Digman, M. A.; Caiolfa, V. R.; Zamai, M.; Gratton, E. The phasor approach to fluorescence lifetime imaging analysis. *Biophys. J.* **2008**, *94*, L14.

(31) Ranjit, S.; Malacrida, L.; Jameson, D. M.; Gratton, E. Fit-free analysis of fluorescence lifetime imaging data using the phasor approach. *Nat. Protoc.* **2018**, *13*, 1979−2004.

(32) Vallmitjana, A.; Torrado, B.; Dvornikov, A.; Ranjit, S.; Gratton, E. Blind resolution of lifetime components in individual pixels of fluorescence lifetime images using the phasor approach. *J. Phys. Chem. B* **2020**, *124*, No. 10126.

(33) Scipioni, L.; Rossetta, A.; Tedeschi, G.; Gratton, E. Phasor S-FLIM: a new paradigm for fast and robust spectral fluorescence lifetime imaging. *Nat. Methods* **2021**, *18*, 542.

(34) Wu, G.; Nowotny, T.; Zhang, Y.; Yu, H.-Q.; Li, D. D.-U. Artificial neural network approaches for fluorescence lifetime imaging techniques. *Opt. Lett.* **2016**, *41*, 2561.

(35) Smith, J. T.; Yao, R.; Sinsuebphon, N.; Rudkouskaya, A.; Un, N.; Mazurkiewicz, J.; Barroso, M.; Yan, P.; Intes, X. Fast fit-free analysis of fluorescence lifetime imaging via deep learning. *Proc. Natl. Acad. Sci. U.S.A.* **2019**, *116*, No. 24019.

(36) Yao, R.; Ochoa, M.; Yan, P.; Intes, X. Net-FLICS: fast quantitative wide-field fluorescence lifetime imaging with compressed sensing-a deep learning approach. *Light: Sci. Appli.* **2019**, *8*, 26.

(37) Verveer, P. J.; Squire, A.; Bastiaens, P. I. Global analysis of fluorescence lifetime imaging microscopy data. *Biophys. J.* **2000**, *78*, 2127.

(38) Straume, M.; Frasier-Cadoret, S. G.; Johnson, M. L. *Topics in Fluorescence Spectroscopy*, Springer, 2002; p 177.

(39) Pelet, S.; Previte, M.; Laiho, L.; So, P. A fast global fitting algorithm for fluorescence lifetime imaging microscopy based on image segmentation. *Biophys. J.* **2004**, *87*, 2807.

(40) Bajzer, Ž.; Therneau, T. M.; Sharp, J. C.; Prendergast, F. G. Maximum likelihood method for the analysis of time-resolved fluorescence decay curves. *Eur. Biophys. J.* **1991**, *20*, 247.

(41) Maus, M.; Cotlet, M.; Hofkens, J.; Gensch, T.; De Schryver, F. C.; Schaffer, J.; Seidel, C. An experimental comparison of the maximum likelihood estimation and nonlinear least-squares fluorescence lifetime analysis of single molecules. *Anal. Chem.* **2001**, *73*, 2078.

(42) Thiele, J. C.; Nevskyi, O.; Helmerich, D. A.; Sauer, M.; Enderlein, J. Advanced data analysis for Fluorescence-Lifetime Single-Molecule Localization Microscopy. *Front. Bioinform.* **2021**, *1*, 56.

(43) Barber, P. R.; Ameer-Beg, S. M.; Pathmananthan, S.; Rowley, M.; Coolen, A. A Bayesian method for single molecule, fluorescence burst analysis. *Biomed. Opt. Express* **2010**, *1*, 1148.

(44) Rowley, M. I.; Barber, P. R.; Coolen, A. C.; Vojnovic, B. *Bayesian Analysis of Fluorescence Lifetime Imaging Data, Multiphoton Microscopy in the Biomedical Sciences XI*, 2011; p 790325.

(45) Rowley, M. I.; Coolen, A. C.; Vojnovic, B.; Barber, P. R. Robust Bayesian fluorescence lifetime estimation, decay model selection and instrument response determination for low-intensity FLIM imaging. *PLoS One* **2016**, *11*, No. e0162224.

(46) Kaye, B.; Foster, P. J.; Yoo, T. Y.; Needleman, D. J. Developing and testing a bayesian analysis of fluorescence lifetime measurements. *PLoS One* **2017**, *12*, No. e0169337.

(47) Wang, S.; Chacko, J. V.; Sagar, A. K.; Eliceiri, K. W.; Yuan, M. Nonparametric empirical Bayesian framework for fluorescence-lifetime imaging microscopy. *Biomed. Opt. Express* **2019**, *10*, 5497.

(48) Santra, K.; Smith, E. A.; Song, X.; Petrich, J. W. A Bayesian approach for extracting fluorescence lifetimes from sparse data sets and its significance for imaging experiments. *Photochem. Photobiol.* **2019**, *95*, 773.

(49) Fazel, M.; Vallmitjana, A.; Scipioni, L.; Gratton, E.; Digman, M. A.; Pressé, S. Fluorescence Lifetime: Beating the IRF and interpulse window. *Biophys. J.* **2023**, *122*, 672.

(50) Ware, W. R.; Doemeny, L. J.; Nemzek, T. L. Deconvolution of fluorescence and phosphorescence decay curves. Least-squares method. *J. Phys. Chem. A* **1973**, *77*, 2038.

(51) Jo, J. A.; Fang, Q.; Papaioannou, T.; Marcu, L. *Laguerre Nonparametric Deconvolution Technique of Time-resolved Fluorescence Data: Application to the Prediction of Concentrations in A Mixture of Biochemical Components, Optical biopsy V*, 2004; p 8.

(52) Campos-Delgado, D. U.; Navarro, O. G.; Arce-Santana, E.; Walsh, A. J.; Skala, M. C.; Jo, J. A. Deconvolution of fluorescence lifetime imaging microscopy by a library of exponentials. *Opt. Express* **2015**, *23*, No. 23748.

(53) Tavakoli, M.; Jazani, S.; Sgouralis, I.; Heo, W.; Ishii, K.; Tahara, T.; Pressé, S. Direct Photon-by-Photon Analysis of Time-Resolved Pulsed Excitation Data using Bayesian Nonparametrics. *Cell Rep. Phys. Sci.* **2020**, *1*, No. 100234.

(54) Le Marois, A.; Labouesse, S.; Suhling, K.; Heintzmann, R. Noise-Corrected Principal Component Analysis of fluorescence lifetime imaging data. *J. Biophotonics* **2017**, *10*, 1124.

(55) Fazel, M.; Jazani, S.; Scipioni, L.; Vallmitjana, A.; Gratton, E.; Digman, M. A.; Pressé, S. High resolution fluorescence lifetime maps from minimal photon counts. *ACS Photonics* **2022**, *9*, 1015.

(56) Stringari, C.; Cinquin, A.; Cinquin, O.; Digman, M. A.; Donovan, P. J.; Gratton, E. Phasor approach to fluorescence lifetime microscopy distinguishes different metabolic states of germ cells in a live tissue. *Proc. Natl. Acad. Sci. U.S.A.* **2011**, *108*, No. 13582.

(57) Li, Y.; Natakorn, S.; Chen, Y.; Safar, M.; Cunningham, M.; Tian, J.; Li, D. D.-U. Investigations on average fluorescence lifetimes for visualizing multi-exponential decays. *Front. Phys.* **2020**, *8*, No. 576862.

(58) Paisley, J.; Carin, L. et al. *Nonparametric Factor Analysis with Beta Process Priors*, Proceedings of the 26th Annual International Conference on Machine Learning, 2009; p. 777.

(59) Al Labadi, L.; Zarepour, M. On approximations of the beta process in latent feature models: Point processes approach. *Sankhya A* **2018**, *80*, 59.

(60) Jazani, S.; Sgouralis, I.; Shafraz, O. M.; Levitus, M.; Sivasankar, S.; Pressé, S. An alternative framework for fluorescence correlation spectroscopy. *Nat. Commun.* **2019**, *10*, No. 3662.

(61) Pressé, S.; Sgouralis, I. *Data Modeling for the Sciences: Applications, Basics, Computations*; Cambridge University Press, 2023.

(62) Rasmussen, C. E. *Summer School on Machine Learning*, Springer, 2003; pp 63−71.

(63) Quiñonero-Candela, J.; Rasmussen, C. E. A unifying view of sparse approximate Gaussian process regression. *J. Mach. Learning Res.* **2005**, *6*, 1939.

(64) Titsias, M. K.; Lawrence, N.; Rattray, M. Markov Chain Monte Carlo Algorithms for Gaussian Processes. *Inference and Estimation in Probabilistic Time-series Models*, 2008; Vol. 9, p 298.

(65) Bryan, J. S., IV; Sgouralis, I.; Pressé, S. Inferring effective forces for Langevin dynamics using Gaussian processes. *J. Chem. Phys.* **2020**, *152*, No. 124106.

(66) Sgouralis, I.; Pressé, S. An introduction to infinite HMMs for single-molecule data analysis. *Biophys. J.* **2017**, *112*, 2021.

(67) Fazel, M.; Wester, M. J.; Mazloom-Farsibaf, H.; Meddens, M.; Eklund, A. S.; Schlichthaerle, T.; Schueder, F.; Jungmann, R.; Lidke, K. A. Bayesian multiple emitter fitting using reversible jump Markov Chain Monte Carlo. *Sci. Rep.* **2019**, *9*, No. 13791.

(68) Jazani, S.; Sgouralis, I.; Pressé, S. A method for single molecule tracking using a conventional single-focus confocal setup. *J. Chem. Phys.* **2019**, *150*, No. 114108.

(69) Fazel, M.; Wester, M. J.; Schodt, D. J.; Cruz, S. R.; Strauss, S.; Schueder, F.; Schlichthaerle, T.; Gillette, J. M.; Lidke, D. S.; Rieger, B.; et al. High-precision estimation of emitter positions using Bayesian grouping of localizations. *Nat. Commun.* **2022**, *13*, No. 7152.

(70) Tavakoli, M.; Jazani, S.; Sgouralis, I.; Shafraz, O. M.; Sivasankar, S.; Donaphon, B.; Levitus, M.; Pressé, S. Pitching single-focus confocal data analysis one photon at a time with Bayesian nonparametrics. *Phys. Rev. X* **2020**, *10*, No. 011021.

(71) Bryan IV, J. S.; Sgouralis, I.; Pressé, S. Diffraction-limited molecular cluster quantification with Bayesian nonparametrics. *Nat. Comput. Sci.* **2022**, *2*, 102.

(72) Saurabh, A.; Fazel, M.; Safar, M.; Sgouralis, I.; Pressé, S. Single-photon smFRET. I: Theory and conceptual basis. *Biophys. Rep.* **2023**, *3*, No. 100089.

(73) Saurabh, A.; Safar, M.; Fazel, M.; Sgouralis, I.; Pressé, S. Single-photon smFRET: II. Application to continuous illumination. *Biophys. Rep.* **2023**, *3*, No. 100087.

(74) Safar, M.; Saurabh, A.; Sarkar, B.; Fazel, M.; Ishii, K.; Tahara, T.; Sgouralis, I.; Pressé, S. Single-photon smFRET. III. Application to pulsed illumination. *Biophys. Rep.* **2022**, *2*, No. 100088.

(75) Metropolis, N.; Rosenbluth, A. W.; Rosenbluth, M. N.; Teller, A. H.; Teller, E. Equation of state calculations by fast computing machines. *J. Chem. Phys.* **1953**, *21*, 1087.

(76) Hastings, W. K. Monte Carlo sampling methods using Markov chains and their applications. *Biometrika* **1970**, *57*, 97.

(77) Murray, I.; Adams, R.; MacKay, D., *Elliptical Slice Sampling*, Proceedings of the Thirteenth International Conference on Artificial Intelligence and Statistics, 2010; p 541.

(78) Davis, R. T.; Blake, K.; Ma, D.; Gabra, M. B. I.; Hernandez, G. A.; Phung, A. T.; Yang, Y.; Maurer, D.; Lefebvre, A. E.; Alshetaiwi, H.; et al. Transcriptional diversity and bioenergetic shift in human breast cancer metastasis revealed by single-cell RNA sequencing. *Nat. Cell Biol.* **2020**, *22*, 310.

(79) Ma, D.; Hernandez, G. A.; Lefebvre, A. E.; Alshetaiwi, H.; Blake, K.; Dave, K. R.; Rauf, M.; Williams, J. W.; Davis, R. T.; Evans, K. T.; et al. Patient-derived xenograft culture-transplant system for investigation of human breast cancer metastasis. *Commun. Biol.* **2021**, *4* (1), 1268.

(80) Liu, L.; Zhang, S. X.; Liao, W.; Farhoodi, H. P.; Wong, C. W.; Chen, C. C.; Ségaliny, A. I.; Chacko, J. V.; Nguyen, L. P.; Lu, M.; et al.

Mechanoresponsive stem cells to target cancer metastases through biophysical cues. *Sci. Transl. Med.* **2017**, *9*, eaan2966.